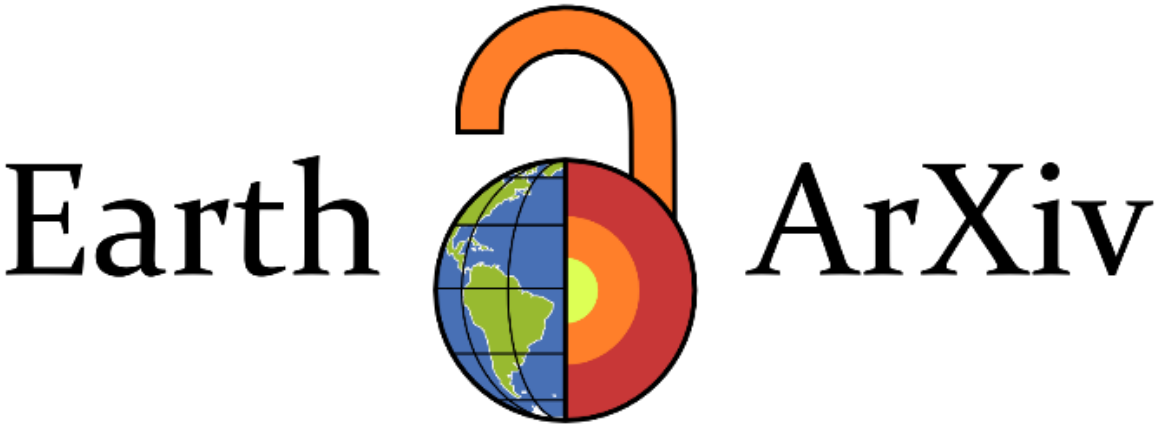

High-Resolution Simulation of the Urban Heat Island Effect in Grenoble During the 2018 Heatwave: Evaluating WRF Model Configurations

Jacobo Gabeiras[1], Chantal Staquet[1], Charles Chemel[2], Alberto Martilli[3]

[1]Université Grenoble Alpes, CNRS, Grenoble INP, LEGI, France
[2]National Centre for Atmospheric Science, NCAS, UK
[3]Centro de Investigaciones Energéticas, Medioambientales y Tecnológicas, CIEMAT, Spain

Email: jacobo.gabeiras@univ-grenoble-alpes.fr

Abstract. This study investigates the Urban Heat Island (UHI) effect in Grenoble, France, during the August 2018 heatwave, using high-resolution Weather Research and Forecasting (WRF) simulations at 111 meters. The objective is to evaluate at this resolution the capacity of different WRF urban parameterizations such as the Building Effect Parameterization (BEP) and Building Energy Model (BEM), to simulate the UHI effect and overall temperature distribution. The validation approach integrates data from official weather stations, crowdsourced Citizen Weather Stations (CWS), and empirical and modeling studies of the UHI in Grenoble. Results show that configurations with advanced urban parameterizations significantly enhance the ability to capture the spatial structure of UHI in urban areas while maintaining strong performance in non-urban regions. However, a trade-off was identified: models that accurately capture the spatial distribution of UHI often exhibit larger errors in absolute temperature predictions, particularly at individual stations. Additionally, all configurations struggled to simulate thermal wind reversals, a key process affecting UHI dynamics in Grenoble's valley. This work highlights the importance of advanced urban parameterizations in improving UHI modeling in complex urban and topographic settings.

1 Introduction

Extreme heat events are known to cause diverse negative impacts on humans. These impacts are most noticeable on both physical (Obradovich et al., 2018) and mental health (Kjellstrom et al., 2016). Worsening sleep quality, reducing human performance and work capacity, and increasing mortality and risk of accidents are the main health impacts from these events. But these events also affect greatly on transport and energy consumption (Chapman et al., 2013).

Extreme heat events are generally characterized by prolonged periods of excessively high temperatures, often referred to as heatwaves. The frequency and intensity of heatwaves are expected to increase due to climate change (Zhang et al., 2012). During these events, the occurrence of tropical night are often common, which is thought to be the temperature at which the body may recover completely over night. Over the course of the 21st century, the number of tropical nights is projected to grow primarily in southern and eastern France (Dhakal et al., 2022). Cities in this region, like Grenoble, are especially vulnerable because of the urban heat island effect (UHI), which intensifies the effects of excessive heat (Oke, 1982).

The Grenoble conurbation offers a unique case study for investigating the urban heat island (UHI) effect in this environment. The complex topography and extensive urban infrastructure of Grenoble, have been show to contribute to the exacerbation of heat events (Foissard & Fouvet, 2022). Studies have attempted methodologies to estimate the UHI of the city with varying methodologies. Xavier Foissard (Foissard & Fouvet, 2022) used a comprehensive geo-statistical model to quantify the UHI during Grenoble's 2020 summer. This model, developed specifically for the Metropolis of Grenoble, estimates the thermal structure by accounting for urban geometry, construction materials, and local temperature measurements.

A different approach was developed by Theeuwes et al. (2017) for calculating the maximum UHI effect expected at each point in the city. Theeuwes' model is a semi-empirical model designed to estimate the maximum Urban Heat Island Intensity (UHI Max) for urban areas in Northwest Europe. It combines physical principles with empirical relationships, integrating meteorological and urban morphological parameters to predict the UHI effect. Specifically, it uses dimensionless analysis (e.g., the Buckingham π theorem) to derive its formulation, making it a simplified yet physically informed approach. While Theewes' model provides a useful and simple framework for estimating UHI intensity, it is important to recognize that the outcomes can be highly sensitive to the input parameters and the characteristics of the calculation setup, including spatial resolution. (Dirksen et al., 2019).

Another example is the one of Marius Zumwald et al. (Zumwald et al., 2021). Their study utilizes a machine learning-based approach to create high-resolution urban temperature maps. This method, applied in Zurich, integrates data from citizen weather stations, open government sources, and remote sensing to train a quantile regression forest algorithm. While this approach is capable of estimating with very high resolution, the efficacy of the model depends heavily on the volume and reliability of data from citizen weather stations. The accuracy and calibration of these data sources can vary considerably, impacting the model's overall effectiveness.

Each approach to UHI modeling, as exemplified by these studies, illustrates the inherent complexities in accurately capturing urban heat dynamics. They offer a method for high resolution temperature estimation and collectively emphasize the critical balance required among the availability and integrity of data. Yet, a notable limitation of these approaches is their limited alignment with fundamental thermodynamic principles. These models often do not fully incorporate essential thermodynamic equations or adhere to established physical laws. Bridging this gap is essential to ensure the reliability and credibility of the outcomes.

The Weather Research and Forecasting (WRF) Model is a powerful tool for urban climate studies. When studying the UHI effect, WRF can be combined with the Building Effect Parameterization (Martilli et al., 2002, BEP) and Building Energy Model (Salamanca et al., 2010, BEM) to better understand temperature changes in cities by incorporating factors such as city layout, buildings, and land use, often resulting in more reliable temperature predictions within urban areas. These parameterizations, were originally designed to operate at rather coarse resolutions (around 500 meters or more) and are used in combination with planetary boundary layer (PBL) schemes, which simulate the vertical transport of heat, moisture, and momentum close to earth's surface.

However, the city of Grenoble presents unique challenges that require much higher resolution simulations. Situated in a Y-shaped valley surrounded by steep mountains, Grenoble's complex topography affects local weather patterns, such as valley winds, temperature gradients, and thermal inversions, which demand a horizontal resolution in the order of 100 meters (Le Bouëdec, 2021). Typically, large eddy simulations (LES) are recommended at these finer resolutions because they explicitly model smaller-scale turbulence. However, BEP and BEM were not originally designed for such high resolution grids. This raises the question of whether these parameterizations can still perform effectively at the finer resolution (111 meters in this case) required for a complex city environment like Grenoble.

To assess the performance of this state of the art model in predicting the UHI effect and temperature distribution in the valley Grenoble, this study examines the August 2018 heatwave. The objective is to assess the accuracy of the results using BEP and BEP+BEM when contrasted with those obtained from WRF without urban parameterization. This study uses the more recent version of BEP+BEM where the module COMFORT has been added. The COMFORT module (Martilli et al., 2024) adds another dimension by incorporating human biometeorological aspects, assessing how urban climate conditions affect human comfort and health.

2 Data and Methods

This study is centered in the Grenoble metropolitan area. Grenoble is the largest city in the Isère department in the Auvergne-Rhône-Alpes region of southeastern France. The population of the Grenoble metropolitan area in 2024 is around 450,000 which makes it the largest metropolis in the Alps (Grenoble Alpes Métropole, 2024). The valley bottom is mostly flat, located at around 200 meters high and it is surrounded by a high mountainous area, with peaks reaching up to 2000 meters in the north and west, and nearly 3000 meters on the east side. This flatness at the bottom of the city surrounded by steep slopes makes this area of great interest as well as challenging from a meteorological modeling standpoint.

WRF version 4.3 is used to perform the meteorological simulations with three-nested domain configuration (fig 1). All three domains have 405 grid cells with a resolution of 9 km for the bigger domain, 1 km for the second one, and 111 meters for the innermost domain. In the vertical dimension, the height of the first mass point is approximately 15 meters. The levels are progressively stretched towards the top, over a total of 91 levels.

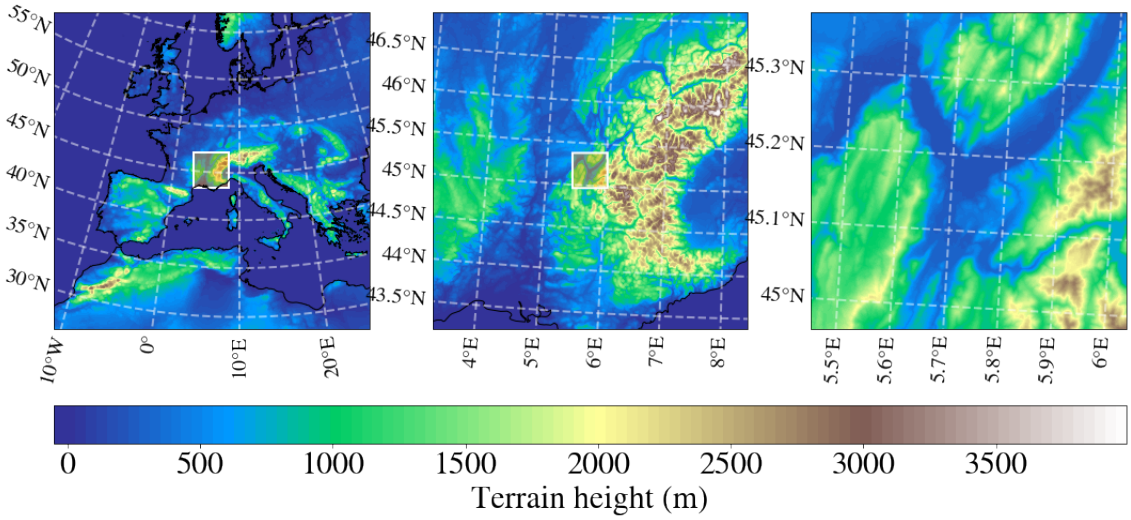

Figure 1: The three nested domains used for the simulations with the numerical model WRF for the 2018 heatwave. ERA5 data at a resolution of 25 km is used to for the forcing.

The BEP+BEM+COMFORT model is used for the urban parameterization. It consists of three key modules, each serving a distinct purpose. BEP (Martilli et al., 2002) focuses on capturing the effects of urban structures on atmospheric variables. It considers the impact of vertical and horizontal surfaces, accounting for factors such as wind speed, temperature, and turbulent kinetic energy. BEP also addresses shadowing and radiation trapping in urban canyons. BEM (Salamanca et al., 2010) enhances the model by estimating building energy consumption. It takes into consideration the effect of air conditioning use, and can resolve the effect of green roofs, solar panels and air conditioning energy demand. The COMFORT module (Martilli et al., 2024) focuses on human comfort within urban areas, considering factors beyond temperature and humidity. It incorporates variables like wind speed, solar radiation, and other meteorological parameters based on international guidelines. Its most recent version also allows for a detailed representation of the tree canopy, where it incorporates the parameterization of the radiative effects of high and low vegetation. This represents and enhancement for accurately capturing the complex urban features, such as buildings, vegetation, and their interactions with temperature dynamics.

The two PBL schemes compatible with the BEP model are the Mellor-Yamada-Janjic (MYJ)

scheme, and the Bougeault and Lacarrere (BouLac) scheme. Noticeable differences in the performance between these schemes have been found mostly during stable periods of inversion (Bi-Hui et al., 2012). The BouLac scheme is chosen for this study as it is the most widely used with BEP+BEM (Martilli et al., 2002; Salamanca et al., 2010).

Care must be given to the representation of the land cover, in particular, the description of the urban surface. The quality of this representation is tightly related to the quality of the results of meteorological variables close to the surface. Here we have made a distinction between the natural and the urban representation. One of the land cover description used in this study is the Corine Land Cover (European Environment Agency, 2020, p. CLC). CLC is a database that consists of an inventory of land cover in 44 classes. It uses a Minimum Mapping Unit of 25 hectares (ha) for areal phenomena and a minimum width of 100 m for linear phenomena. The classes in this inventory are aggregated into five main classes: water bodies, wetlands, forests, seminatural areas, agricultural areas, and artificial surfaces. These need to be remmaped into USGS clases (USGS, 2022, United States Geological Survey). Table AT1 explains the remapping scheme. When using WRF without and urban squeme such as BEP or BEP+BEM the urban classes of CLC when remapped into USGS classes are: 31 "LR" (Low Residential), 32 "HR" (High Residential), and 33 "I" (Industrial). The way WRF simulates the presence of these classes is by assuming a fixed urban fraction for each class of 50%, 90% and 95% by default. This assumption can however be inaccurate.

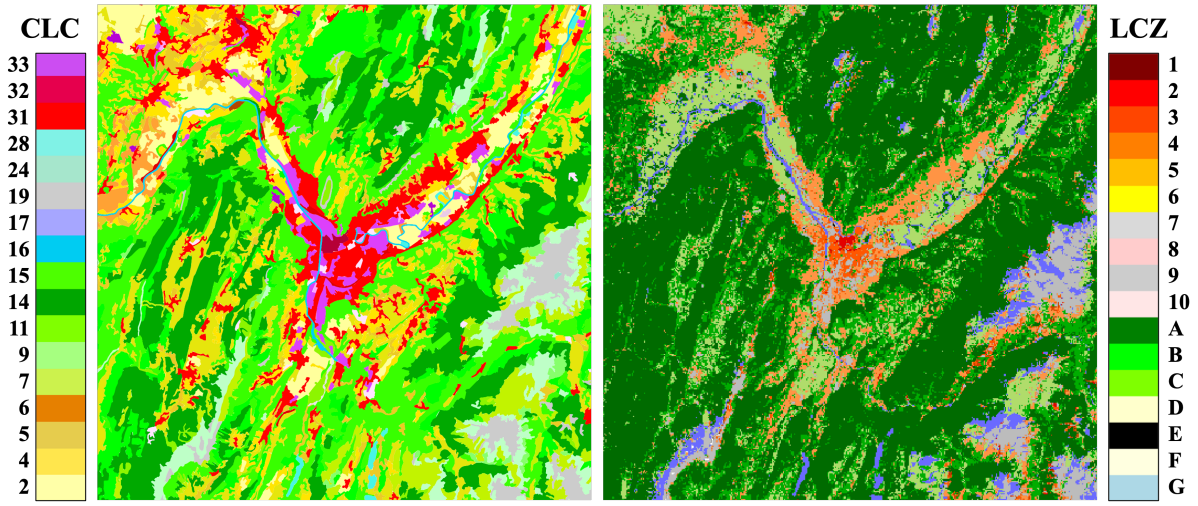

Figure 2: Comparison of the Land cover output using the Corine Land Cover EU database (European Environment Agency, 2020) (left) and the LCZ generator product (Demuzere et al., 2021) (right). The color legend for the CLC map corresponds to the remapped values of the USGS land description (See Table AT1).

In contrast, WRF simulations using the BEP and BEP+BEM+COMFORT models allow for the incorporation of detailed urban data such as Local Climate Zones (LCZ), urban fraction, albedo values, and other urban characteristics. This approach replaces the CLC data with LCZ representation. The WUDAPT (World Urban Database and Access Portal Tools) project (Demuzere et al., 2019) provides an innovative method for generating LCZs in urban areas, offering a finer urban classification based on thermal, geometric, and radiative properties. Unlike the broad CLC classification tailored for Europe, WUDAPT focuses on detailed urban characteristics through a community-driven, crowdsourced approach. Two tools from WUDAPT were adequate for this study: the global raster file (Demuzere et al., 2019), which offers a broad view of LCZs worldwide, and the LCZ generator (Demuzere et al., 2021), an interactive tool for cre-

ating detailed maps for specific cities. For this study, the LCZ generator was chosen. A detailed representation of the different local climate zones of the city is very useful to tabulate unknown data of the city needed for the modelization, such as the thermal properties of building materials, or the usage properties of Air Conditioning systems. However, when it comes to urban parameters such as the building heights and surface fraction, urban canopy parameterizations such as BEP+BEM allow for the ingestion of the gridded map if available. Although this approach presents several challenges in the data gathering and reprocessing compared to the traditional LCZ based approach, which relies in table values, it results in a more accurate representation of the urban settlement. Detailed building data, is obtained from the OpenStreetMaps Building API (OSM Buildings, 2024, Application Programming Interface). This data is then crossed with building height data from the World Settlement Footprint 3D database (Esch et al., 2022, WSF3D). The preprocessing of this datasets for the area of interest includes the calculation of planar surface ratio, total surface ratio, average building height, and distribution of building heights within each grid cell. High and low egetation cover data are sourced with the help of the Grenoble Region Urban Planning Agency (AURG) from the CoSIA database of the Institut national de l'information géographique et forestière (IGN, 2023, IGN).

The atmospheric forcing used for the model is ECMWF Reanalysis v5 (ERA5) hourly data on pressure levels (C3S, 2018a) and ERA5 hourly data on single levels (C3S, 2018b).

2.1 The heatwave episode

According to Perkins and Alexander (2013), heatwaves are defined as periods during which the weather remains extremely hot for an extended duration, typically several consecutive days. When it comes to heatwave identification, the definition of a heatwave varies depending on the context of the study and the specific impacts being assessed, with studies using a variety of approaches, such as hard threshold, percentile based threshold or the Excess Heat Factor approach, or EHF (Kapwata et al., 2022; Mason et al., 2022; Tong et al., 2010). In the context of heatwaves affecting human health, it is common in the literature to require a minimum duration of at least three consecutive days, combined with percentile-based thresholds for both minimum (Tmin) and maximum (Tmax) temperatures (Perkins & Alexander, 2013). The definition used for the selection of the episode is a period of at least three consecutive days during which both maximum and minimum temperatures are equal to or above their respective 92nd percentile within the historical months from May to October, inclusive.

The specific event considered in this evaluation is the heatwave that occurred in July-August 2018. This heatwave lasted from the 31st of July to the 6th of August. The identification of this heatwave was conducted by analyzing historical temperature data from the Institut Laue-Langevin (ILL) meteorological station. Due to computational cost and the high resolution needed for this study, only three days are simulated spanning from the 31st of July to the 3rd of August.

3 Results

In this study, a comparison is made between the performance of four different WRF configurations. Run 1 with a 3D TKE closure without a PBL nor urban canopy parameterization. Run 2 also with no urban canopy parameterization and the BouLac PBL scheme (Bougeault & Lacarrere, 1989). Run 3 applies the BEP model with the BouLac PBL scheme. Finally, Run 4 uses the BEP+BEM configuration with the BouLac PBL scheme to evaluate an advanced urban setup. An overview of the configuration for each run, including the PBL schemes utilized, is shown in Table 1. The set up of each configuration is designed to utilize the full potential of its

capabilities. This includes using a LCZ based land use description for BEP and BEM as oposed to CLC based description as well as the use of urban parameters at the level of the grid cell and high and low vegetation description data for the most advance configuration (Run 4).

Table 1: Summary of the four simulation configurations used to assess model performance in Grenoble. Each setup varies in its use of planetary boundary layer (PBL) schemes and urban parameterizations. Urban morphology and vegetation data are only included in runs with BEP or BEM. H. Smagorinsky Tands for Horizontal Smagorinsky turbulence scheme.

No.	Acronym	PBL Scheme	Turbulence Scheme	Urban Model	Land Use	Urban Parameters	Vegetation Data
Run 1	NoPBL–NoUrban	No PBL	3D TKE closure	No	CLC	No	No
Run 2	PBL–NoUrban	BouLac	H. Smagorinsky	No	CLC	No	No
Run 3	PBL–BEP	BouLac	H. Smagorinsky	BEP	LCZ	Yes	No
Run 4	PBL–BEM	BouLac	H. Smagorinsky	BEP+BEM	LCZ	Yes	Yes

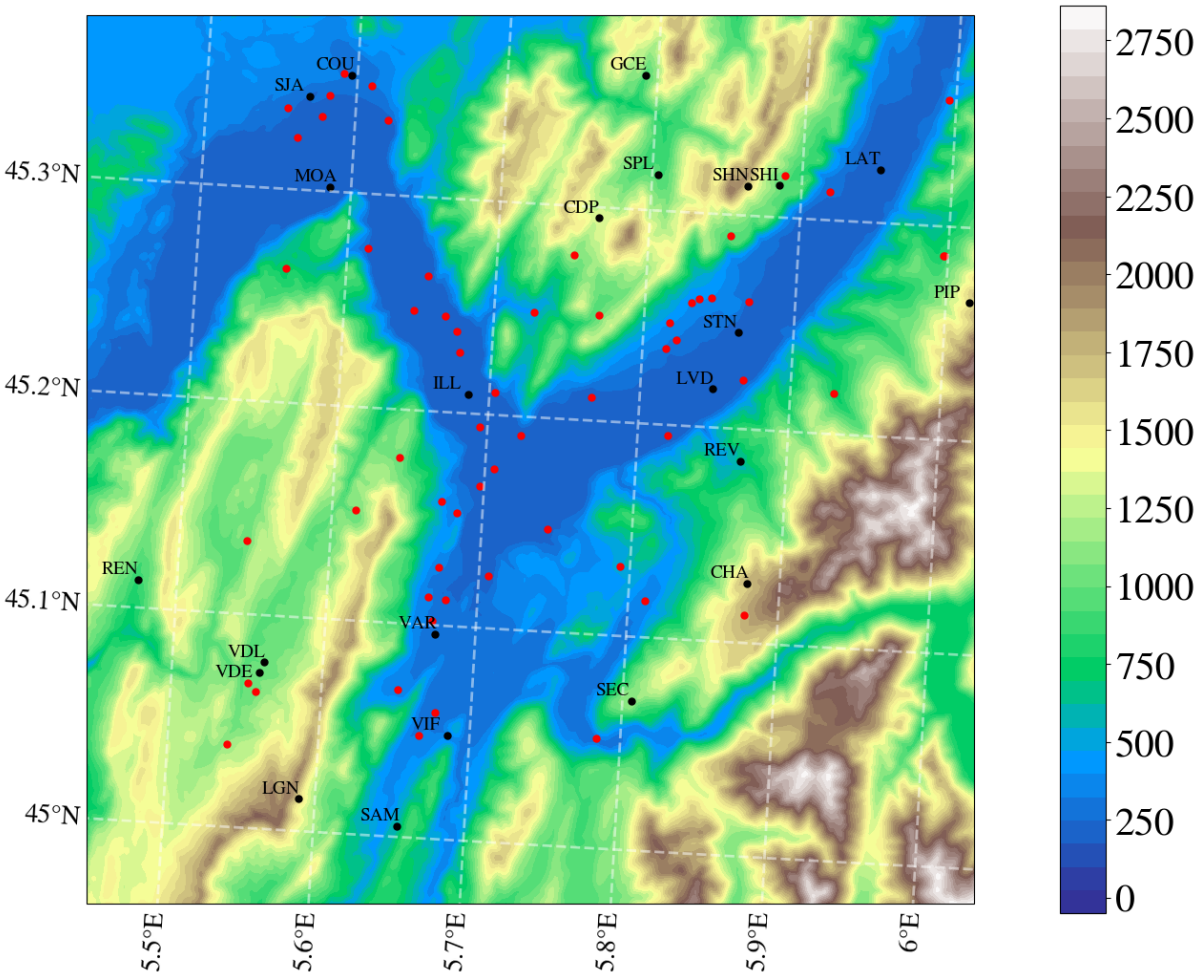

Figure 3: Location of the 23 meteorological stations from Météo France (Météo-France, 2024) denoted with black dots. The red dots mark the location of the 60 crowd-sourced stations (Netatmo, 2024). The colorbar indicates the height of the terrain in meters.

Each simulation is assessed based on its capacity to estimate the temperature distribution in the valley as well as authentically replicate the phenomenon of UHI effect. Special emphasis

is placed on Grenoble due to its central location within the metropolitan area, dense population and its heightened experience of the UHI effect in comparison to neighboring cities.

Firstly, in Section 3.1, the validation of the temperature maps is conducted by comparing them with actual temperature data from multiple locations (Figure 3). This analysis focuses on assessing the spatial hourly diurnal bias and correlation between the simulation results and the measurements obtained from the Météo France meteorological stations network (Météo-France, 2024). Subsequently, in Section 3.2, an examination of temperature variations between Grenoble and a rural area outside its valley, specifically Moirans, is carried out to account for the UHI temporal estimation. The temperature difference between these two locations is computed time interval during the third night of the episode. This distribution trend is then compared with measurements from meteorological stations in both Grenoble (ILL) and Moirans (MOA). Continuing with the analysis, in Section 3.3, detailed temperature maps are generated to depict the UHI effect within Grenoble (Figure 6) and the Metropolis of Grenoble (Figure 7). These maps are qualitatively compared with the respective Urban Heat Island maps from a 2020 summer study (Foissard & Fouvet, 2022). The output is compared with the UHI extracted from readings at 60 crowd-sourced meteorological stations. Lastly, in Section 3.4 the results of the simulations are compared with the application of the semi-empirical model from Theeuwes et al. (2017) to the region of this study.

3.1 Temperature Bias and Correlation with Temperature Measurements

The evaluation of spatial temperature distribution is conducted through an hourly bias and correlation analysis with measurements from the 23 meteorological weather stations (Figure 4) for a period spanning from July 31 to August 3, 2018. Throughout the observation period, all simulation configurations demonstrated a diurnal pattern in correlation values, with higher correlations during daylight hours reaching up to 0.98 at midday hours and lower correlations at night, dipping down to 0.75 at 5 am (UTC), indicative of the increase in thermal heterogeneity due to solar heating effects (Figure 4). The results also show an overestimation of night time temperatures (+0.5 °C in average) and an underestimation of daytime temperatures (-1.8 °C in average). It is important to note that only five of weather stations are located in urban areas. This distribution of stations suggests that the analysis predominantly assesses the models' overall capability to simulate the meteorology across all land settings rather than urban-specific phenomena. The first 7 hours of the simulation are not taken into account as they are considered spin up time.

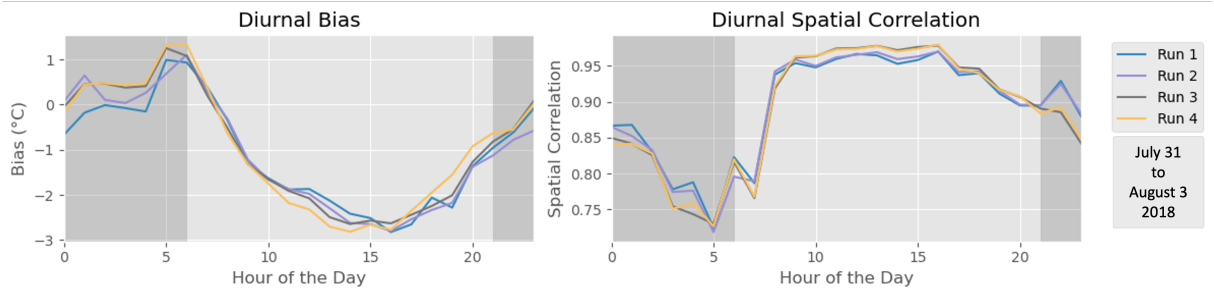

Figure 4: Hourly Spatial Bias and Correlation Coefficients with Meteorological Measurements from July 31 to August 3, 2018. The graph displays the temporal evolution of spatial correlation between modeled and observed temperatures at 23 weather stations. The lines represent five different simulation configurations: Run 1 (NoPBL–NoUrban, blue), Run 2 (PBL–NoUrban, purple), Run 3 (PBL-BEP, grey), Run 4 (PBL-BEM, yellow). Shaded areas indicate nighttime, highlighting the diurnal variation in correlation.

All models correlate spatially similarly with the measurements. The NoPBL–NoUrban configuration maintains generally the lowest correlation during the day, although highest during the night compared to the others, while the urban model configurations display varying degrees of enhancement in spatial correlation.

Run 2 and Run 3 share the same turbulence parameterization, and despite an increased complexity in the urban corfiguration, there is no observable change in the performance regarding valley-scale spatial correlation. Similarly, between Run 3 and Run 4, the main variation lies in the inclusion of an urban energy model and additional urban descriptors in Run 4 (PBL-BEM), yet this does not alter their performance in valley-scale spatial correlation.

Since there are only five Météo France stations located in urban areas (Table AT2), the evaluation primarily reflects the models' capability to simulate meteorological conditions across a mix of land types, rather than focusing specifically on urban phenomena such as the UHI effect. To address this limitation, Section 3.3 presents UHI maps compared with measurements gathered from crowd-sourced meteorological stations, allowing for a more detailed assessment of the models' performance in urban settings.

3.2 UHI temporal estimation

One key feature when evaluating a model's performance on Urban Heat Island estimation is the magnitude and temporal variability. Two stations have been chosen for the calculation of this effect: ILL station representing the urban environment, as it is the official station closest to the city center, and Moirans station (MOA) representing the rural environment. Figure 3 provides a visualization of the geographical locations of Grenoble and Moirans. ILL at 208 meters and MOA at 191 meters are closely at the same height, thus no height bias is taken into account. The temperature difference between the grid cells where these stations are located is calculated to estimate the UHI effect as predicted by the model.

Figure 5 presents a comparative analysis of the four different model runs in Table 1 simulating the UHI effect, using the temperature difference between a meteorological station ILL and MOA as a benchmark. The progress from Run 1 through Run 4, shows a clear trend of increasing accuracy in the models, as evidenced by the improving correlation coefficients. Notably, Run 4 (PBL-BEM) shows the highest degree of accuracy with a correlation of 0.88 and the lowest MAE of 0.96°C for the period of three days and nights considered. Run 3 (PBL-BEP), achieves also a high correlation of 0.86 MAE of 1.27°C.

While the results on the UHI temporal evolution show close resemblance with the UHI recorded, as stated in the previous section, the absolute temperature trends tend to deviate from the real measures where they typically underestimate the temperatures during the day and underestimate during the night. This comes to show that there is a trade-off between spatial and temporal accuracy across the different model configurations. While Run 4 (PBL-BEM) performs the best at estimating the UHI trend, accurately capturing the relative temperature differences between urban (ILL) and rural (MOA) stations, it struggles with the absolute temperature predictions for each station individually. In terms of temporal MAE and correlation, Run 4 ranks among the worst-performing configurations for these two stations, consistently underestimating temperatures and showing a smaller range of diurnal variation. Conversely, Run 1 (NoPBL–NoUrban) demonstrates the best performance for station-specific temperature predictions, achieving the lowest MAE and highest correlation for each station separately. However, this configuration performs poorly when it comes to the spatial aspect, failing to capture the UHI trend. The contrasting performance of these configurations underscores the difficulty in achieving a balance between spatial accuracy, such as the urban-rural temperature contrast critical for UHI studies, and temporal accuracy, which is essential for capturing the diurnal temperature cycle and overall temperature absolute values at individual stations.

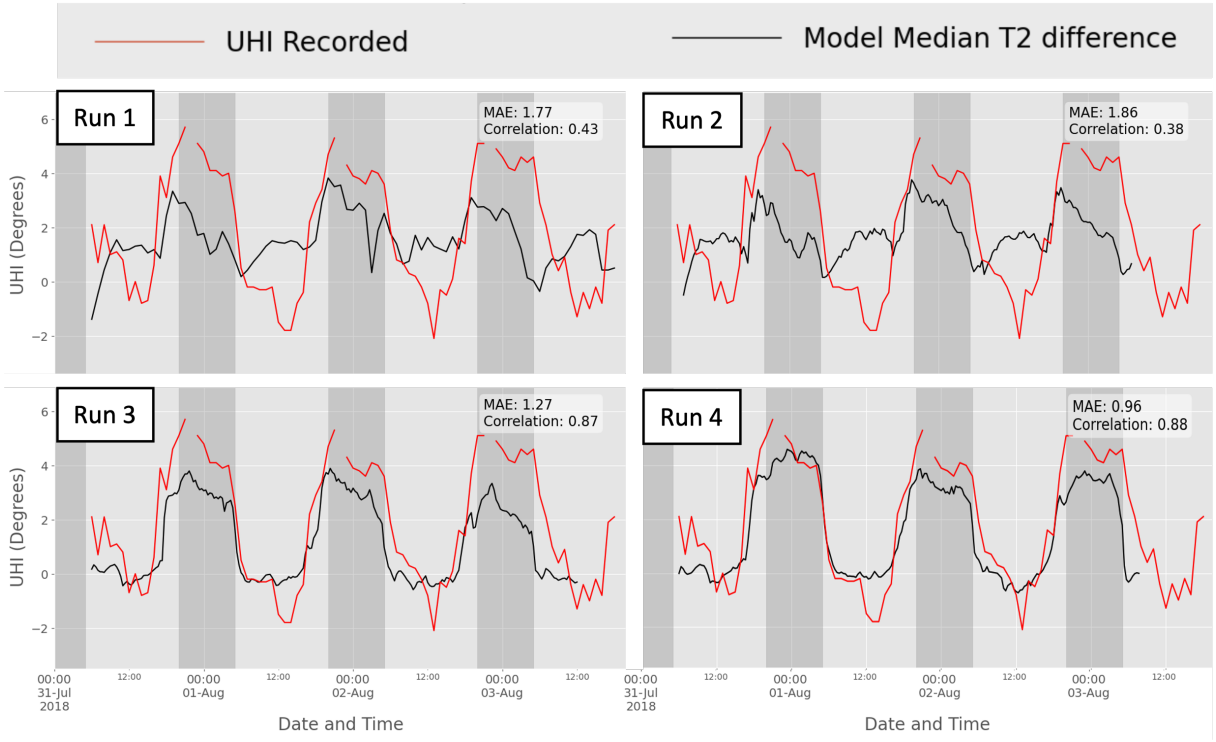

Figure 5: Urban Heat Island effect visualizations for five different simulation runs of Table 1. The red line is the temperature difference between ILL and Moirans stations, and the black signal is the model estimation for the difference in temperature between ILL and MOA locations. (Top left) Run 1: Non-Urban Model for baseline comparison. (Top right) Run 2: BEP with default parameters to assess a generic urban configuration. (Bottom left) Run 3: BEP with BouLac PBL scheme. (Bottom right) Run 4: BEP+BEM+COMFORT. This sequence highlights the enhanced detail and variation captured as the model configurations become more complex.

3.3 UHI spatial estimation

In this section, a comparative qualitative analysis of the UHI effect in Grenoble is performed, based on the simulations of the four different configurations. The analysis focuses on the night of August 3rd, 2018, as it marks the final night of the simulation and is considered to provide the most reliable results. This choice accounts for the time required for certain variables, particularly those related to the ground, such as soil moisture and ground temperature, to stabilize during the spin-up period. Figure 6 reveals distinct variations in the thermal impact of urban structures.

Figure 6 shows a comparison of UHI simulations for different modeling configurations centered on Grenoble. Runs 1 and 2, as illustrated in the top left of the figure, do not quite capture the typical UHI structure. The urban warming effect is not well defined, and the temperature gradient is much less pronounced, especially compared to the later configurations.

Runs 3 PBL-BEP and Run 4 PBL-BEM exhibit a UHI effect more aligned with the study from 2020 (Foissard & Fouvet, 2022) (bottom right panel), though they still exhibit some differences. These runs demonstrate a stronger, more concentrated UHI effect with temperatures exceeding 4°C in the densest urban areas. While this resembles a typical UHI pattern, as seen in past studies, it is important to account for event-specific factors such as the valley wind flow, which can affect the distribution and intensity of urban heating. This aspect is further addressed in Section 4.

Figure 7 compares UHI estimates from five different model configurations during the heat-

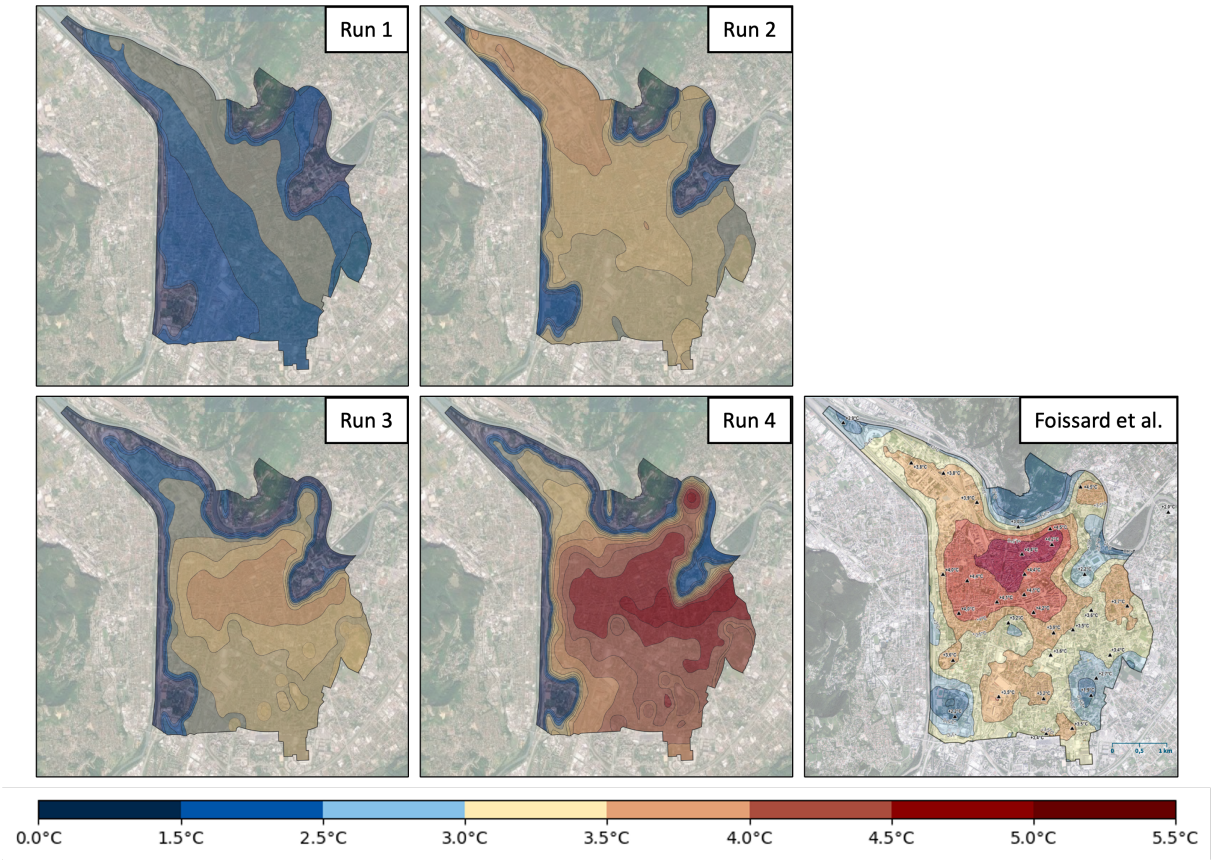

Figure 6: Comparison of UHI estimates, for the night of August 3rd 2018, for different modeling configurations focused on the city of Grenoble. (Top left) Run 1 NoPBL–NoUrban, (Top middle) Run 2 PBL–NoUrban model, (Bottom left) Run 3 PBL-BEP model, (Bottom middle) Run 4 PBL-BEM, and (Bottom right) UHI study (Foissard & Fouvet, 2022) for the heatwave of 2020 as a reference. The visualizations illustrate the spatial temperature variations and the UHI effect, with the color legend displaying the magnitude of the UHI.

wave in Metropolis of Grenoble. Runs 1 and 2 (NoPBL–NoUrban and PBL–NoUrban) fail to capture the UHI structure effectively, showing much cooler temperatures and an under representation of urban warming. Runs 3 and 4 (PBL-BEP and PBL-BEM) closely align with the large scale structure of the UHI observed (bottom right) in the reference study by Xavier Foissard (Foissard & Fouvet, 2022).

3.3.1 Validation of the UHI Estimation with Citizen Weather Stations (CWS)

Due to the scarcity of official weather stations in urban areas, this study leverages data from Citizen Weather Stations (CWS) using a crowdsourcing approach to validate the UHI estimations. CWS networks, such as those provided by Netatmo, are installed by individuals across a variety of locations, offering real-time and historical weather data, including temperature, humidity, and wind speed. This approach has been proven useful for urban climate studies, such as the UHI effect, where a dense spatial resolution of temperature measurements is critical (Fenner et al., 2021; Meier et al., 2017).

The raw data, covering the period from 2013 to 2023, was retrieved via the Netatmo API (Netatmo, 2024), providing a rich dataset for analysis. However, the data quality from CWS can vary significantly due to inconsistent sensor placement, exposure to environmental elements,

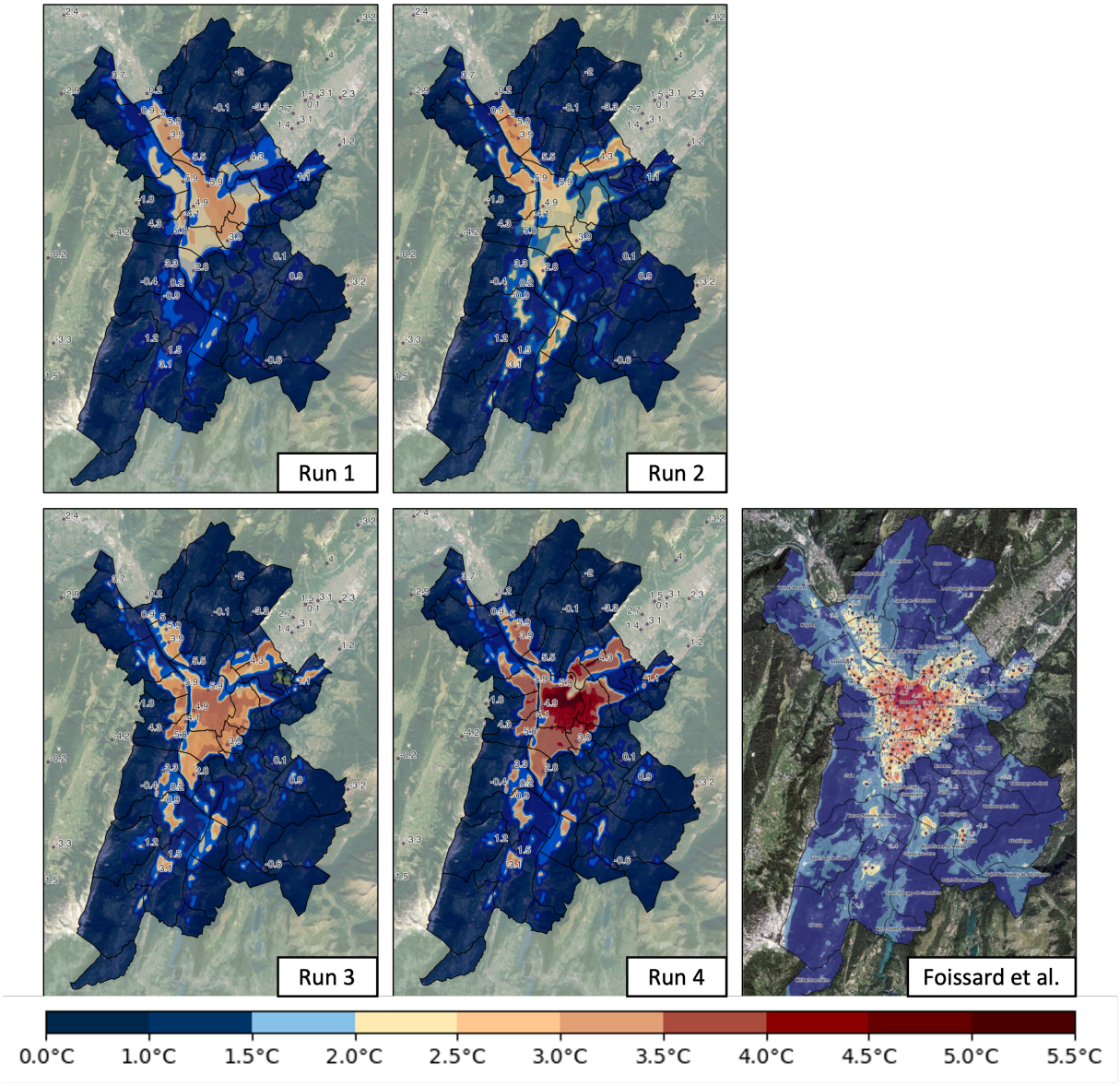

Figure 7: Like Figure 6 but for the Metropolitan area. (Top left) Run 1 NoPBL–NoUrban, (Top middle) Run 2 PBL–NoUrban model, (Bottom left) Run 3 PBL-BEP, (Bottom middle) Run 4 PBL-BEM model, and (Bottom right) UHI study (Foissard & Fouvet, 2022) for the heatwave of 2020 as a reference. The visualizations illustrate the spatial temperature variations and the UHI effect, with the color legend displaying the magnitude of the UHI. The maps have been overlayed with the UHI estimation from readings at each crowd-sourced meteorological station.

and occasional device malfunctions (Fenner et al., 2021). To address these potential issues, a rigorous data filtering process was applied, similar to the methodology outlined by Meier et al. (2017). This process includes various levels of filtering based on metadata validation, data availability, and error detection due to sensor misplacement or radiative errors. The filtering results are summarized in Table AT4, which provides an overview of the quality levels, criteria used for filtering, potential error sources, and the percentage of raw data that met each criterion. After filtering, only 32.9% of the initial dataset was deemed suitable for inclusion in the UHI analysis. Finally, from the 265 valid stations, only 60 were active during the selected episode.

This final set of filtered data was used to validate the UHI estimation from different WRF

model configurations, ensuring that only high-quality, reliable data contributed to the analysis. Figure AF2 illustrates the temperature measurements across all CWS over the 10-year period from 2013 to 2023, highlighting the seasonal patterns and variability in raw data, with significant dispersion due to the presence of outliers and inconsistent data. The comparison between raw and filtered data shows the improvement after applying the data filtering process.

In Figure 8, the performance of the various WRF model runs is compared against the filtered CWS data for both non-urban and urban areas. The left panel shows the spatial correlation between the modeled and observed temperatures, while the right panel illustrates the MAE. The exact values can be found in Table 2.

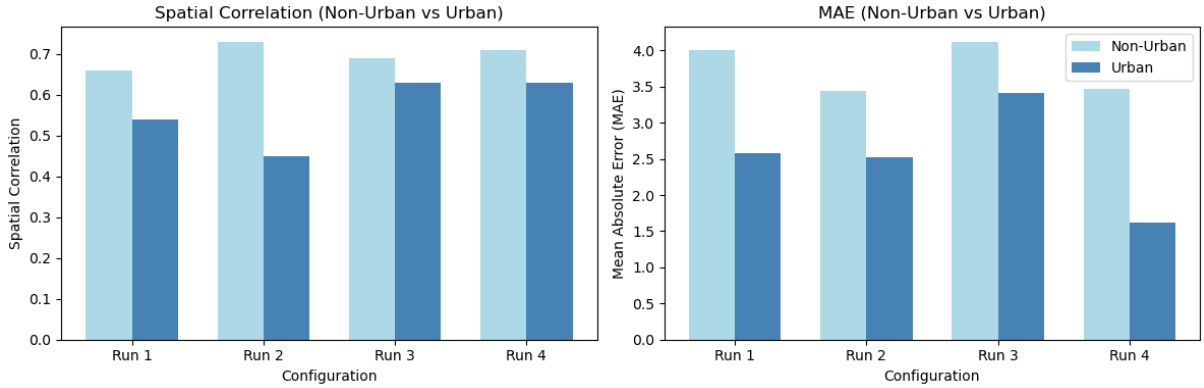

Figure 8: Comparison of Spatial Correlation and MAE for different WRF model configurations in both Non-Urban and Urban areas, validated against data from Citizen Weather Stations (CWS). Out of the 60 CWS stations, 25 are located in natural cells and 35 in urban cells.

The spatial correlation analysis reveals that Run 2 (PBL–NoUrban) achieves the highest spatial correlation in non-urban areas, with a correlation of 0.73, but its performance declines in urban regions, with 0.45. Run 4 (PBL-BEM), on the other hand, maintains a more balanced performance, achieving 0.71 in non-urban and 0.63 in urban areas, showcasing the potential of incorporating detailed urban energy models for more accurate UHI simulation. Interestingly, Run 1 (NoPBL–NoUrban) performs well in non-urban areas, with a spatial correlation of 0.66 and an MAE of 4.01, but struggles in capturing the spatial correlation of the UHI effect in urban areas, where the correlation is 0.54 and the MAE is 2.58.

Overall, the comparison highlights that while certain configurations, like Run 2, excel in non-urban settings, the complexity of urban environments, such as those found in Grenoble, requires more advanced urban-specific models like BEP+BEM (Run 4) to capture the full extent of the UHI phenomenon. This analysis suggests the importance of selecting appropriate model configurations based on the intended study focus, as spatial resolution and the inclusion of urban energy models significantly influence the simulation outcomes.

3.4 UHI Max spatial Estimation

This section presents the spatial estimation of the maximum UHI effect, utilizing Theeuwes et al. empirical UHI formula (Theeuwes et al., 2017) as a reference. The Maximum Urban Heat Island intensity (UHI Max) is a measure of the greatest temperature difference between an urban area and its surrounding rural environment, typically occurring during the nighttime or early morning. By integrating key meteorological data with urban form parameters, such as the Sky View Factor (SVF) and vegetation cover (vegf), this method provides a baseline for comparing the UHI dynamics within Grenoble. The resulting UHI max map, illustrated in Figure 8, is used

as a reference to evaluate the different modeling configurations applied in this study. This allows for a comprehensive comparison between the empirical model and the high-resolution numerical simulations.

This method integrates routine meteorological data with urban form factors to predict the daily maximum UHI following the expression below:

$$UHI_{\max}^{Th} = M_{rural}(2 - SVF - veg_f) \tag{1}$$

where M_{rural} encapsulates meteorological variables external to the urban environment, SVF represents the Sky View Factor within urban street canyons, and veg_f is the fractional vegetation cover within a 500m radius, determined via satellite imagery. The variable M_{rural} is defined by the expression:

$$M_{rural} = \frac{1}{4}\sqrt[4]{\frac{DTR^3 \cdot S}{U}} \tag{2}$$

with DTR as the diurnal temperature range, S the mean solar irradiance over 24 hours, and U the daily mean wind speed at 10 meters above ground level. The comprehensiveness of this model allows for its application beyond mere UHI estimation, extending to broader urban meteorological inquiries.

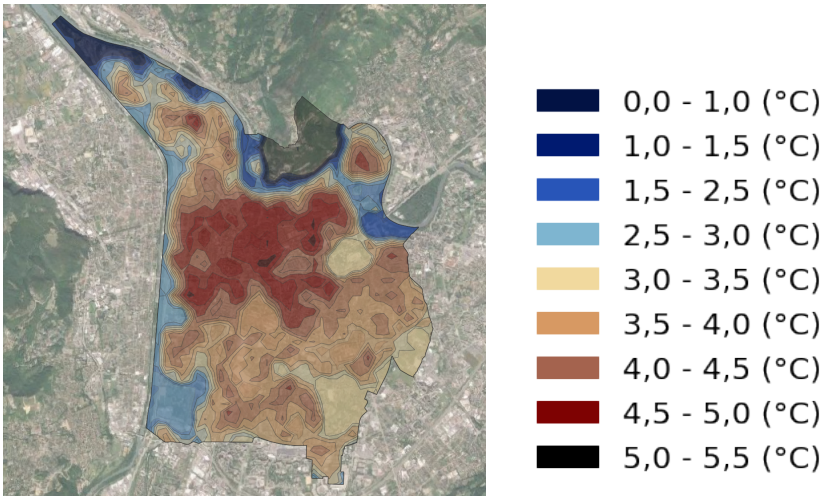

Figure 9: Reference UHI max based on Theeuwes' UHI equation (Theeuwes et al., 2017), used for comparative baseline.

Using ILL station data for the calculation of Mrural we conduct a comparison between UHI_{max} estimations derived from Theeuwes' model and those obtained from the different configurations. To achieve this, the correlation is computed between Theeuwe's model output and each simulation of temperature at both 2 meters (T2) and 20 meters for the Grenoble area.

Figure 10 shows the correlation between the Theeuwes' UHI model and each run. The correlation is evaluated at two heights: 2 meters, and 20 meters. The first one refers to variable T2 while the second is the model level temperature interpolated at 20. The exact values can be found in Table 2. The correlation at 2 meters tends to be higher for all runs than it is at 20 meters, showing the highest correlation for Runs 3 and 4 (0.71 and 0.72 respectively). The high correlation is due to the sudden transitions of T2 between urban and non urban areas. As a result, there is a stronger correlation at 2 meters than at 20 meters. At 20 meters, Run 3 has a correlation of 0.31 and Run 4 exhibits strong performance, with a correlation of 0.47, while

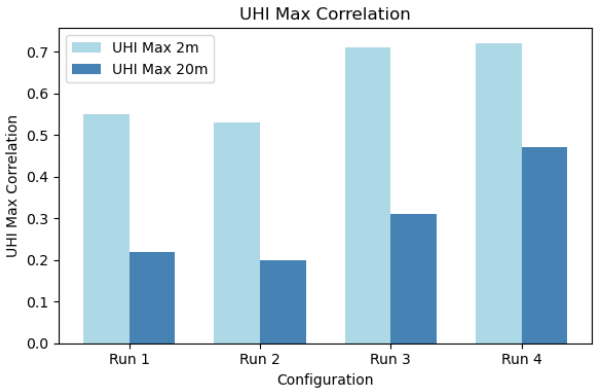

Figure 10: Correlation of UHI Max at 2 meters (left) and 20 meters (right) for different simulation configurations. The figure illustrates the correlation between modeled UHI maxima and the UHI reference values derived from Theeuwes' UHI model, comparing the accuracy at two heights: 2 meters and 20 meters.

Runs 1 and 2 (NoPBL–NoUrban and PBL–NoUrban) show lower correlations (0.22 and 0.20 respectively).

This analysis shows that configurations incorporating urban parameterization, such as BEP and BEM, demonstrated a stronger ability to capture the UHI Max expected from the Theeuwes' UHI semi-empirical model, indicating that incorporating detailed urban features like building energy and vegetation effects leads to more accurate UHI simulations. Table 2 sumarizes the main validation results obtained in Section 3.3 and 3.4

Table 2: Spatial Correlation and MAE for Urban and Non-Urban Areas, and Correlation of UHI Max (Netatmo CWS and Theeuwes' model).

	CWS – Spatial Correlation		CWS – MAE		UHI Max Correlation (Theeuwes)	
Configuration	Non-Urban	Urban	Non-Urban	Urban	UHI Max 2 m	UHI Max 20 m
Run 1	0.66	0.54	4.01	2.58	0.55	0.22
Run 2	0.73	0.45	3.44	2.52	0.53	0.20
Run 3	0.69	0.63	4.12	3.42	0.71	0.31
Run 4	0.71	0.63	3.47	1.62	0.72	0.47

4 Valley Wind Analysis

In mountainous regions like Grenoble, the valley wind dynamics are critically important due to the complex interaction between the large-scale synoptic winds and the local topographical effects. Two main types of wind systems are typically observed: thermally-driven winds and mechanically-driven winds. In a valley like Grenoble's Y-shaped configuration, these wind systems interact in a way that heavily influences both the local weather (Largeron & Staquet, 2016) and urban climate phenomena, including the UHI effect (Foissard & Fouvet, 2022).

Thermally-driven winds, such as slope and valley winds, develop due to temperature differences between the air at different elevations. During the day, up-slope and up-valley winds are generated as the sun heats the valley floor, causing the air to rise. At night, this process reverses, and cooler down-slope and down-valley winds occur as the ground cools faster than the air above it. These winds are especially relevant during heatwaves when the diurnal temperature variation becomes more pronounced.

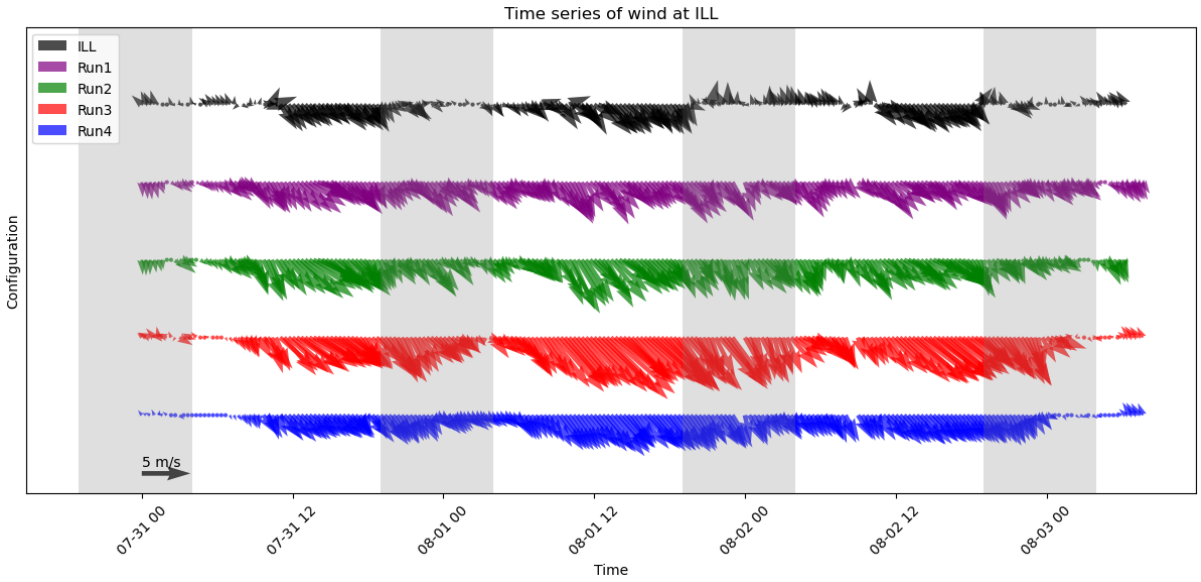

Figure 11: Time series of wind speed and direction at the ILL station for the period between July 31st and August 2nd, 2018, showing comparisons between observed data (ILL) and five different WRF model configurations (Runs 1-4) with a time interval of 20 minutes. Wind speed is represented by the length of the arrows, with the direction indicating the flow direction. The shaded areas represent nighttime hours.

Mechanically-driven winds, on the other hand, are a result of the interaction between large-scale synoptic winds and the topographical constraints of the valley. These winds, known as forced channeling, occur when synoptic winds align with the valley axis, pushing air down the valley. This type of wind can affect the local wind patterns and temperature distributions.

As Figure 12 illustrates, the wind structure in Grenoble's valley remains relatively consistent across different WRF simulations, regardless of the turbulence scheme used. This consistency suggests that the steep, narrow valley walls constrain the development of convective cells, limiting variability across runs. However, an important discrepancy across all simulations is their inability to capture the wind reversal phenomenon observed in the valley, which is driven by thermal winds.

This wind reversal, identified in the ILL station (Figure 11), is particularly significant because it can alter the UHI structure (Foissard & Fouvet, 2022). During nighttime cooling, cool air from the northwest flows down the valley and can push the warmer urban air to the opposite side, reshaping the UHI footprint. The failure of models to capture this reversal at the location of ILL station is a notable limitation, as it affects the accuracy of UHI simulation in the city. Despite this, wind direction and speed are well captured at the locations of the stations LVD and PdC which, in the Y-shaped valley, represent the eastern and southern valley flow (see Figure 3).

In conclusion, while the models show consistent wind patterns due to the topographical constraints of the valley, capturing dynamic phenomena like wind reversals is critical for accurately modeling urban climate, particularly during heatwave events. This limitation highlights the need for further refinement of the model's capacity to simulate thermally-driven winds in complex terrain settings.

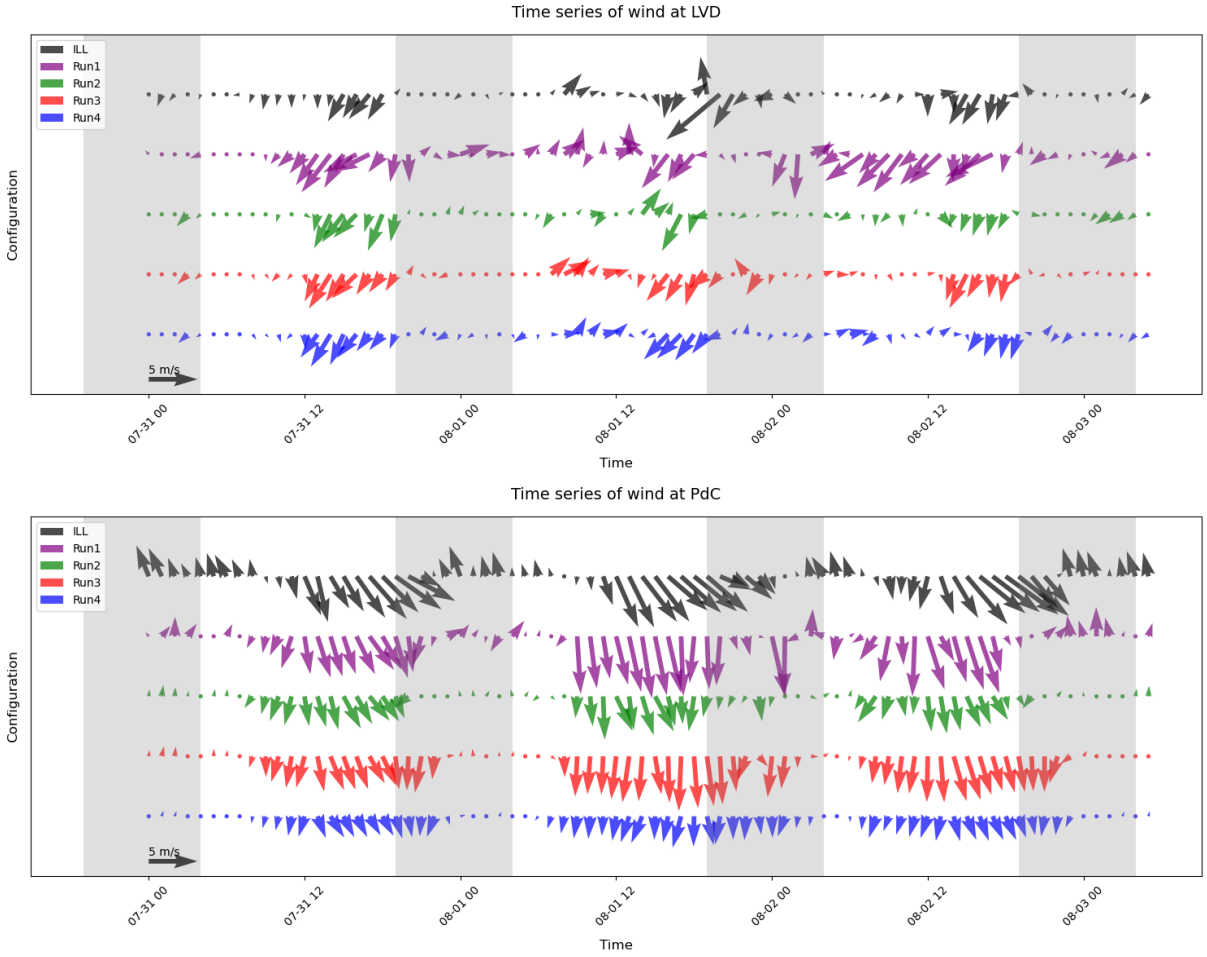

Figure 12: Time series of wind speed and direction at the LVD and PdC stations for the period between July 31st and August 2nd, 2018, showing comparisons between observed data and the four different WRF model configurations (Runs 1-4) with a time interval of 1 hour.

5 Conclusions

The study aimed to assess the capacity of various WRF model configurations to simulate the Urban Heat Island (UHI) effect in Grenoble during the August 2018 heatwave, with a particular focus on high spatial resolutions of 111 meters. The motivation was to determine whether these configurations, originally designed for coarser grids, could still perform effectively at finer resolutions.

Validation using Citizen Weather Stations (CWS) highlighted the added value of crowd-sourced temperature measurements, particularly in dense urban areas where official weather stations coverage is limited. After rigorous filtering, 60 high-quality CWS were retained, providing detailed spatial coverage that was instrumental in evaluating UHI patterns. Their inclusion helped validate the spatial structure of the UHI across Grenoble's urban zones, complementing the 23 Météo-France stations used primarily for temporal assessment of MAE and spatial Pearson's correlation.

The results demonstrated that, at the experiment's high resolution, the ability to capture local temperature variations, particularly in complex urban environments, varied depending on the configuration. Configurations incorporating detailed urban schemes, such as BEP and BEM, performed far better in capturing the UHI spatial structure compared to simpler, non-urban

setups. The best-performing configuration (Run 4: BEP+BEM) achieved the lowest urban MAE of 1.62 °C and the highest spatial correlation of 0.63. In contrast, the BouLac-only setup (Run 2) showed higher MAE (2.10 °C) and lower correlation (0.45), while the NoPBL–NoUrban configuration (Run 1) captured local variability but failed to reproduce the spatial pattern of the UHI. This highlights the importance of advanced urban parameterizations, as spatial resolution alone is not sufficient to account for the complex thermal, radiative, and wind dynamics unique to cities.

A trade-off between spatial and temporal accuracy was observed. While Run 4 (PBL-BEM) captured the overall UHI trend and maintained good spatial correlation, it showed higher errors in predicting absolute temperatures at individual stations, with a temperature MAE of 2.09 °C. Conversely, Run 1 (NoPBL–NoUrban) provided more accurate point-based temperature variations (MAE of 1.95 °C), especially at those at lower altitudes (see Table AT3), but its lack of urban parameterization resulted in poor spatial correlation (0.54 as opposed to 0.63 for run 4) and inadequate representation of urban thermal contrasts. This trade-off emphasizes the challenge of achieving both accurate spatial representation of urban-rural temperature differences and reliable temperature estimates at station level.

Despite the high resolution of the experiment set up, all configurations faced challenges in accurately simulating wind patterns, particularly the wind reversal observed in the valley during the heatwave, which typically happens during summer nights and early mornings. This phenomenon, driven by thermal wind effects, can influence the UHI structure. None of the configurations, regardless of turbulence scheme, effectively captured this dynamic, suggesting that further refinement is needed in how wind patterns interact with urban form in these models.

In conclusion, this study confirms that high-resolution modeling is possible for accurately representing the UHI effect, especially in complex urban settings like Grenoble. The study proves that simulations with urban parameterizations, such as BEP and BEP+BEM, are not only possible but encouraged when it comes to accurately simulating the Urban Heat Island effect. Resolution alone does not ensure accuracy. Capturing urban-rural thermal contrasts also requires proper representation of urban morphology, energy exchanges, and wind–terrain interactions. Future work should focus on improving these components—especially the coupling between thermal and wind dynamics—to further advance urban climate modeling in complex terrains.

6 Appendix Chapter

Corine Land Cover (CLC)		United States Geological Survey (USGS)	
ID	Description	ID	Description
1.1.1	Continuous urban fabric	32	High Intensity Residential
1.1.2	Discontinuous urban fabric	31	Low Intensity Residential
1.2.1	Industrial or commercial units	33	Industrial or Commercial
1.2.2	Road and rail networks	33	Industrial or Commercial
1.2.3	Port areas	33	Industrial or Commercial
1.2.4	Airports	33	Industrial or Commercial
1.3.1	Mineral extraction sites	19	Barren or Sparsely Vegetated
1.3.2	Dump sites	19	Barren or Sparsely Vegetated
1.3.3	Construction sites	19	Barren or Sparsely Vegetated
1.4.1	Green urban areas	7	Grassland
1.4.2	Sport and leisure facilities	7	Grassland
2.1.1	Non-irrigated arable land	2	Dryland Cropland and Pasture
2.1.2	Permanently irrigated land	3	Irrigated Cropland and Pasture
2.1.3	Rice fields	3	Irrigated Cropland and Pasture
2.2.1	Vineyards	6	Cropland/Woodland Mosaic
2.2.2	Fruit trees and berry plantations	6	Cropland/Woodland Mosaic
2.2.3	Olive groves	6	Cropland/Woodland Mosaic
2.3.1	Pastures	2	Dryland Cropland and Pasture
2.4.1	Annual crops	6	Cropland/Woodland Mosaic
2.4.2	Complex cultivation patterns	4	Mixed Dryland/Irrigated Cropland
2.4.3	Agricultural land	5	Cropland/Grassland Mosaic
2.4.4	Agro-forestry areas	6	Cropland/Woodland Mosaic
3.1.1	Broad-leaved forest	11	Deciduous Broadleaf Forest
3.1.2	Coniferous forest	14	Evergreen Needleleaf Forest
3.1.3	Mixed forest	15	Mixed Forest
3.2.1	Natural grasslands	7	Grassland
3.2.2	Moors and heathland	9	Mixed Shrubland/Grassland
3.2.3	Sclerophyllous vegetation	9	Mixed Shrubland/Grassland
3.2.4	Transitional woodland-shrub	9	Mixed Shrubland/Grassland
3.3.1	Beaches, dunes, sands	19	Barren or Sparsely Vegetated
3.3.2	Bare rocks	19	Barren or Sparsely Vegetated
3.3.3	Sparsely vegetated areas	19	Barren or Sparsely Vegetated
3.3.4	Burnt areas	19	Barren or Sparsely Vegetated
3.3.5	Glaciers and perpetual snow	24	Snow or Ice
4.1.1	Inland marshes	17	Herbaceous Wetland
4.1.2	Peat bogs	17	Herbaceous Wetland
4.2.1	Salt marshes	17	Herbaceous Wetland
4.2.2	Salines	17	Herbaceous Wetland
4.2.3	Intertidal flats	17	Herbaceous Wetland
5.1.1	Water courses	16	Water Bodies
5.1.2	Water bodies	28	Water Bodies
5.2.1	Coastal lagoons	28	Water Bodies
5.2.2	Estuaries	16	Water Bodies
5.2.3	Sea and ocean	16	Water Bodies

Table AT1: Scheme used to map the Urban Classes from CLC into the USGS categories.

Station Name	Height (m)	Latitude	Longitude	Land Class		Class Description
MOIRANS-AREA	191	45.302	5.586	USGS	5	Cropland/Grassland Mosaic
GRENOBLE - ILL -CEA	208	45.209	5.686	LCZ	6	Open Low-Rise
ST-M-D'HERES-GALOCHERE	220	45.168	5.767	LCZ	6	Open Low-Rise
GRENOBLE - LVD	220	45.218	5.848	USGS	7	Grassland
ST-NAZAIRE-AREA	230	45.245	5.863	USGS	5	Cropland/Grassland Mosaic
LA TERRASSE-AREA	238	45.325	5.952	USGS	7	Grassland
VARCES-ALLIERES-ET-RISSE-AREA	271	45.096	5.673	LCZ	6	Open Low-Rise
ST JEAN DE MOIRANS-AREA	290	45.344	5.569	LCZ	5	Open Mid-Rise
COUBLEVIE	300	45.355	5.596	USGS	19	Barren or Sparsely Vegetated
VIF-AREA	356	45.049	5.685	USGS	11	Deciduous Broadleaf Forest
MEYLAN	469	45.229	5.778	USGS	11	Deciduous Broadleaf Forest
SAINT-MARTIN-DE-LA-CLUZE-AREA	580	45.005	5.655	USGS	4	Mixed Dryland
REVEL-EDF	645	45.185	5.869	LCZ	6	Open Low-Rise
LIVET-EDF	695	45.112	5.957	USGS	15	Mixed Forest
MONTAUD-EDF	740	45.263	5.561	USGS	4	Mixed Dryland
RENCUREL-EDF	885	45.113	5.474	USGS	2	Dryland Cropland and Pasture
RENCUREL	885	45.113	5.474	USGS	2	Dryland Cropland and Pasture
GRANDE-CHARTREUSE	945	45.363	5.792	USGS	15	Mixed Forest
GRANDE CHARTREUSE-EDF	945	45.363	5.792	USGS	15	Mixed Forest
ORNON	950	45.052	5.987	USGS	7	Grassland
ST-PIERRE-LES EGAUX	950	45.317	5.804	USGS	2	Dryland Cropland and Pasture
SAINT-HILAIRE_SAPC	990	45.315	5.885	USGS	7	Grassland
VILLARD-DE-LANS	1027	45.078	5.561	USGS	2	Dryland Cropland and Pasture
VILLARD-DE-LANS-EDF	1050	45.073	5.558	USGS	7	Grassland
AUTRANS	1069	45.182	5.552	USGS	7	Grassland
LAVALDENS	1070	44.991	5.883	USGS	2	Dryland Cropland and Pasture
SECHILIENNE-EDF	1120	45.07	5.806	USGS	11	Deciduous Broadleaf Forest
COL DE PORTE-EDFNIVO	1325	45.295	5.766	USGS	14	Evergreen Needleleaf Forest
COL DE PORTE-EDF	1325	45.295	5.766	USGS	14	Evergreen Needleleaf Forest
COL DE PORTE-NIVOSE	1325	45.295	5.765	USGS	15	Mixed Forest
PIPAY_SAPC	1578	45.265	6.016	USGS	14	Evergreen Needleleaf Forest
LE GUA-NIVOSE	1646	45.015	5.589	USGS	19	Barren or Sparsely Vegetated
CHAMROUSSE	1730	45.128	5.878	USGS	7	Grassland
ST HILAIRE-NIVOSE	1756	45.314	5.864	USGS	19	Barren or Sparsely Vegetated

Table AT2: Table of meteorological stations used for comparison.

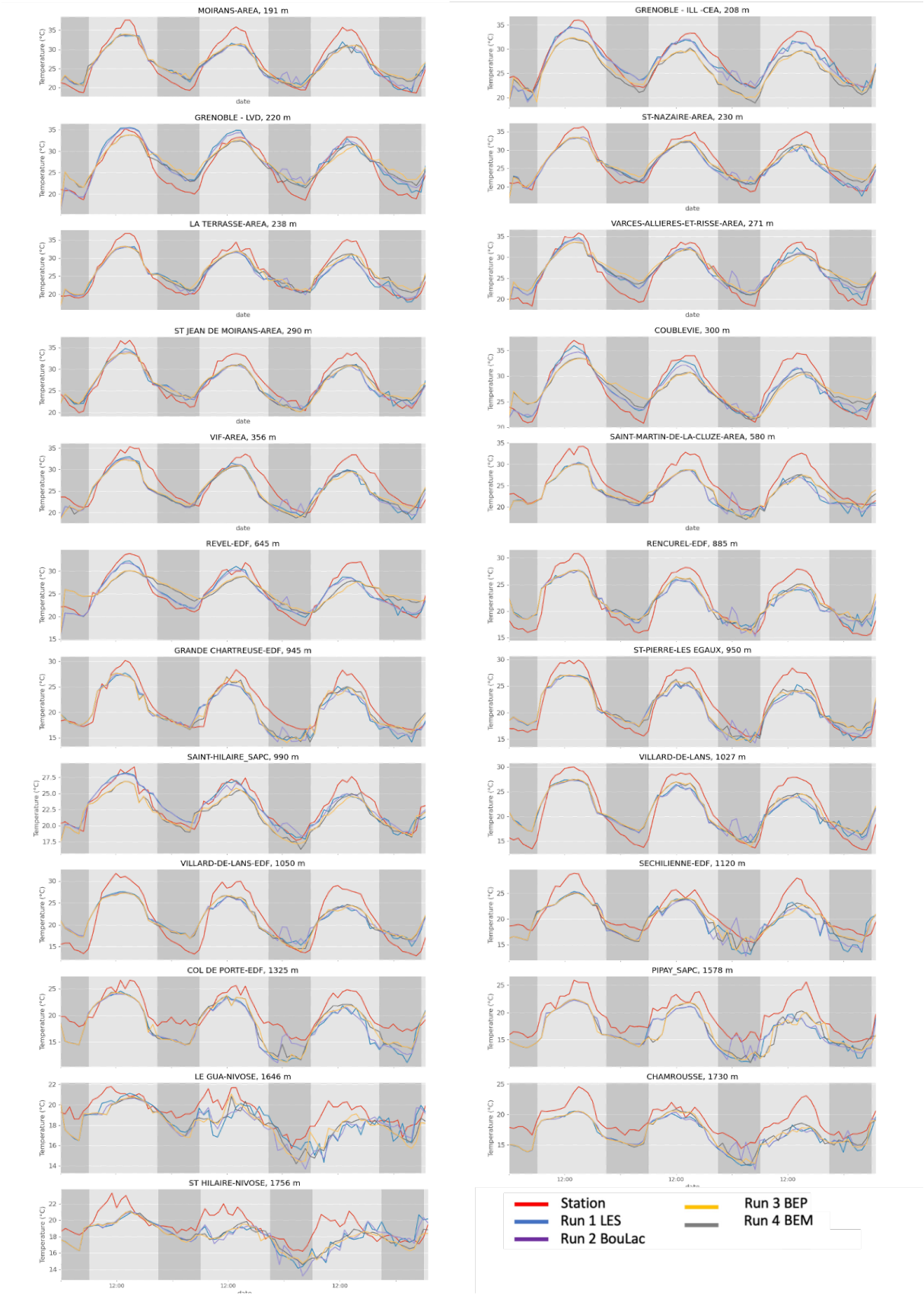

Figure AF1: Temperature trends at each of the 23 meteorological stations with the outputs of the 5 different runs for comparison.

Station	**Alt**	Corr / MAE **Run 1**	Corr / MAE **Run 2**	Corr / MAE **Run 3**	Corr / MAE **Run 4**
MOIRANS-AREA	191	0.96 / 1.95	0.96 / 2.1	0.96 / 2.04	0.95 / 2.16
GRENOBLE - ILL -CEA	208	0.95 / 1.15	0.95 / 1.22	0.95 / 2.35	0.93 / 2.27
GRENOBLE - LVD	220	0.94 / 1.88	0.94 / 1.82	0.94 / 1.94	0.91 / 2.32
ST-NAZAIRE-AREA	230	0.94 / 1.81	0.94 / 1.82	0.96 / 1.71	0.94 / 1.97
LA TERRASSE-AREA	238	0.96 / 1.74	0.96 / 1.76	0.97 / 1.69	0.96 / 1.86
VARCES-ALLIERES-ET-RISSE-AREA	271	0.96 / 1.72	0.96 / 1.83	0.95 / 2.07	0.93 / 2.36
ST JEAN DE MOIRANS-AREA	290	0.94 / 1.64	0.95 / 1.65	0.95 / 1.58	0.94 / 1.76
COUBLEVIE	300	0.96 / 1.27	0.96 / 1.48	0.90 / 2.16	0.84 / 2.48
VIF-AREA	356	0.89 / 2.18	0.89 / 2.2	0.90 / 2.25	0.89 / 2.16
SAINT-MARTIN-DE-LA-CLUZE-AREA	580	0.94 / 2.54	0.93 / 2.5	0.95 / 2.28	0.93 / 2.27
REVEL-EDF	645	0.93 / 1.3	0.92 / 1.39	0.81 / 2.51	0.77 / 2.62
RENCUREL-EDF	885	0.92 / 2.05	0.92 / 2.09	0.94 / 1.89	0.93 / 1.94
GRANDE CHARTREUSE-EDF	945	0.90 / 1.82	0.91 / 1.71	0.93 / 1.46	0.92 / 1.53
ST-PIERRE-LES EGAUX	950	0.92 / 2.03	0.93 / 2.01	0.95 / 1.81	0.94 / 1.93
SAINT-HILAIRE_SAPC	990	0.93 / 0.91	0.93 / 0.92	0.94 / 1.33	0.94 / 1.29
VILLARD-DE-LANS	1027	0.91 / 2.45	0.92 / 2.55	0.93 / 2.24	0.93 / 2.26
VILLARD-DE-LANS-EDF	1050	0.91 / 2.97	0.90 / 3.14	0.91 / 2.85	0.91 / 2.86
SECHILIENNE-EDF	1120	0.86 / 2.36	0.84 / 2.36	0.90 / 1.92	0.89 / 1.83
COL DE PORTE-EDF	1325	0.88 / 2.88	0.85 / 2.76	0.90 / 2.41	0.89 / 2.47
PIPAY_SAPC	1578	0.90 / 2.87	0.89 / 2.66	0.88 / 2.78	0.89 / 2.79
LE GUA-NIVOSE	1646	0.65 / 1.21	0.72 / 1.41	0.78 / 1.29	0.82 / 1.26
CHAMROUSSE	1730	0.89 / 2.33	0.85 / 2.18	0.89 / 2.07	0.88 / 2.17
ST HILAIRE-NIVOSE	1756	0.52 / 1.54	0.51 / 1.54	0.68 / 1.38	0.67 / 1.45
Average	–	0.89 / 1.94	0.89 / 1.96	0.91 / 2.00	0.90 / 2.09

Table AT3: MAE and Correlation (Corr) for different model configurations at each station.

Quality level	**Criteria for data filtering**	**Potential error sources**	**% of raw data**
A0	Crowdsourced air temperature (Tcrowd) raw data with correct timestamp		100
A1	Netatmo stations with valid metadata (latitude, longitude)		99.5
A2	80% hourly data per day	Intermittent failure of wireless network, loss of battery power, server failure	97.2
A3	80% daily data per month	User-specific installation error (misuse), Netatmo outdoor module set up indoors	81.7
B	Indoor station filter, monthly average and standard deviation of daily minimum air temperature (TN)	Netatmo outdoor module set up in a sunlit location (no radiation shield)	39.5
C1	Systematic radiative error filter, positive and significant correlation between global radiation and air temperature difference (Tcrowd_ID – Tref)	Netatmo outdoor module received direct shortwave radiation	35.4
C2	Single value radiative error filter, flagging daytime values when air temperature difference (Tcrowd_ID – Tref) $> 3 \times$ SD in Tref	Netatmo outdoor module temporarily moved, other measurement errors	32.9
D	Outlier filter based on spatial average of Tcrowd $\pm$ 3 $\times$ SD in Tcrowd	Netatmo API and server limits, user-specific operating error	30.4

Table AT4: Quality levels, criteria for data filtering, potential error sources, and percent of raw data

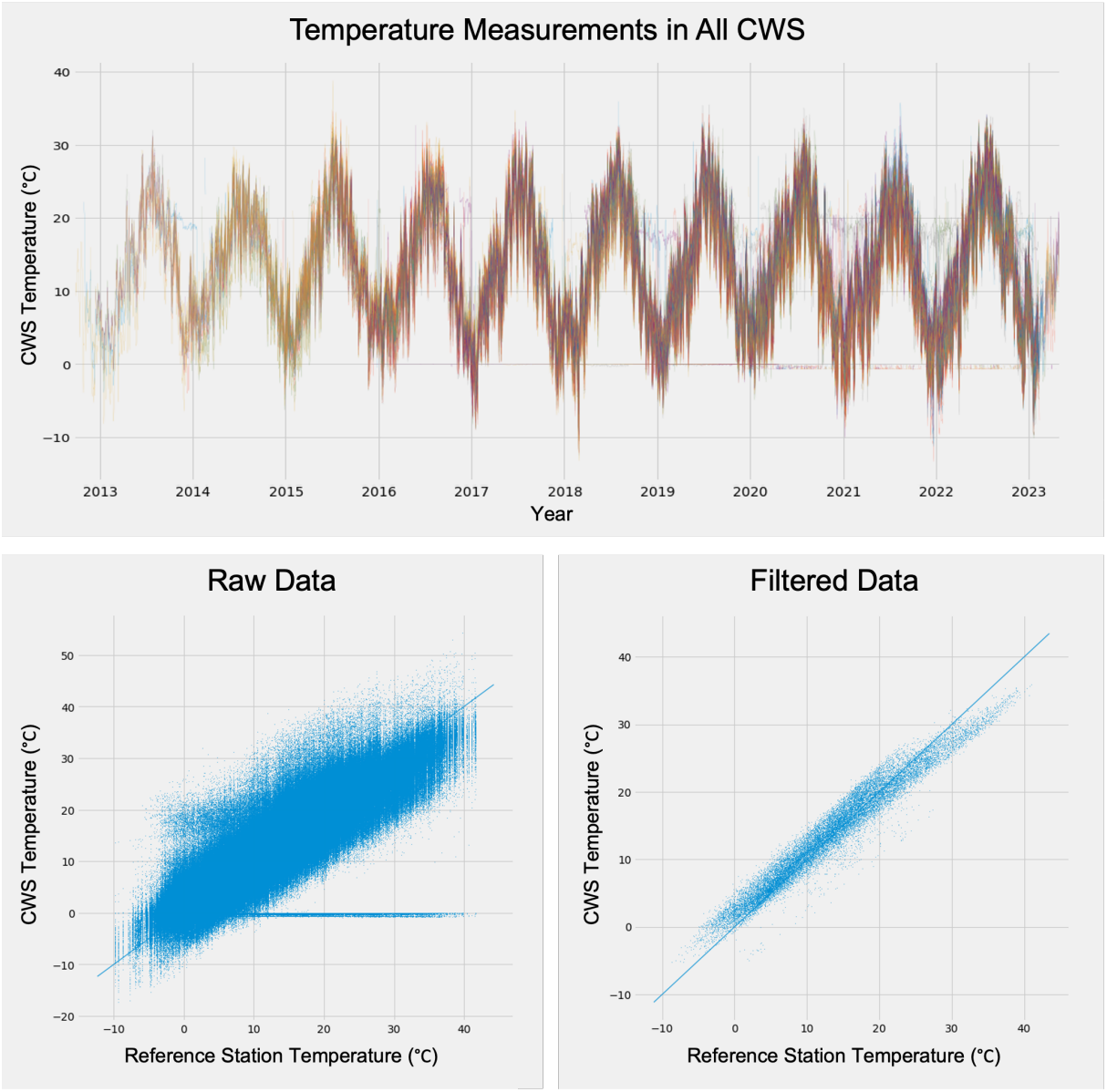

Figure AF2: Overview of temperature data from Citizen Weather Stations (CWS) spanning the years 2013 to 2023. The top panel shows the raw temperature measurements from all available CWS, highlighting the seasonal variations over the 10-year period. The bottom left panel compares the raw CWS temperature data against reference station temperatures. The bottom right panel shows the same comparison after applying the filtering process.

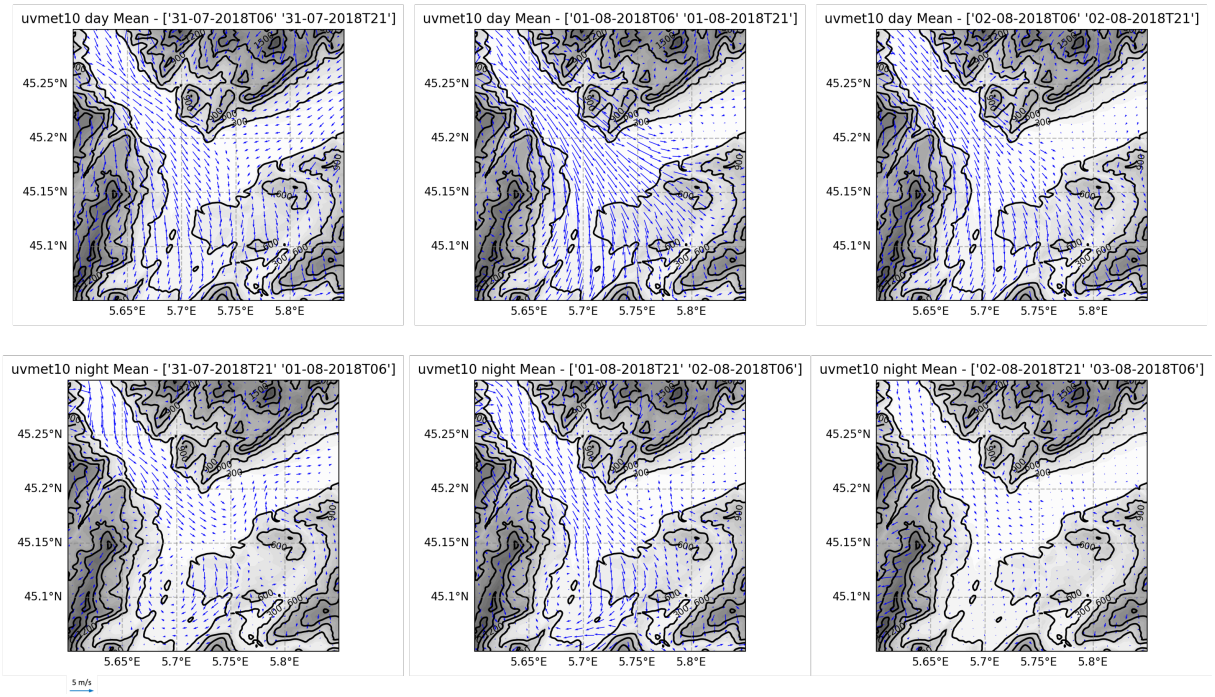

Figure AF3: Wind maps for Run 1 (NoPBL–NoUrban) showing the day and night mean wind patterns for three consecutive days during the heatwave event.

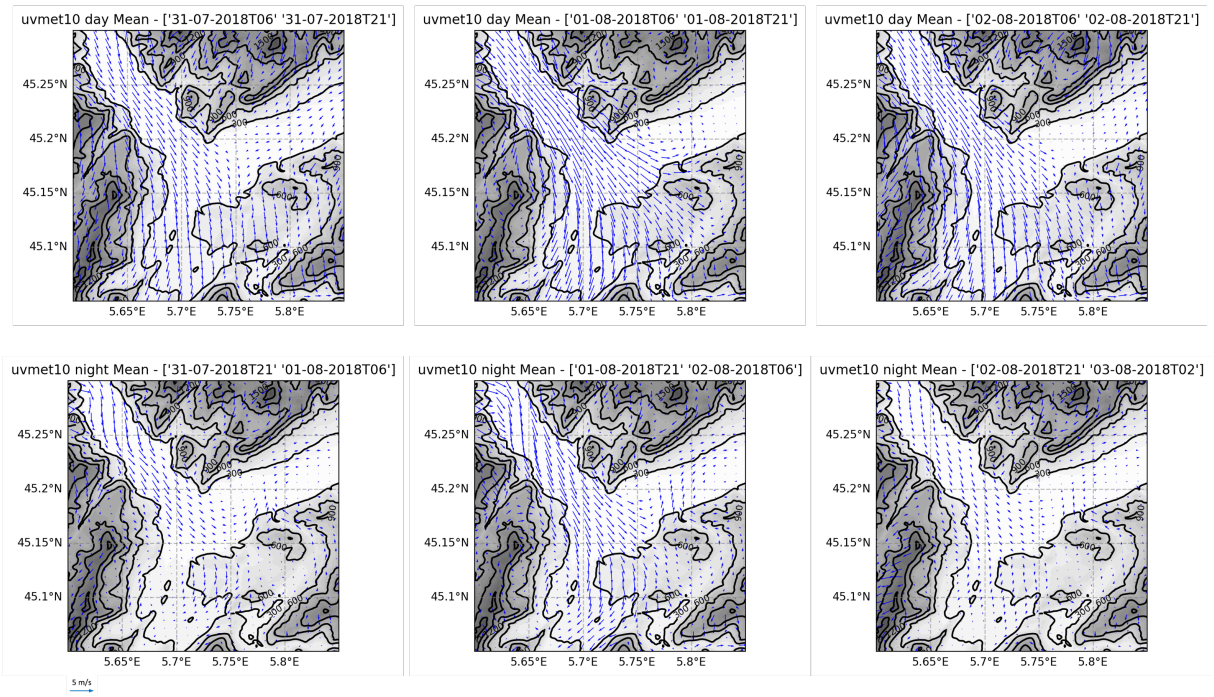

Figure AF4: Wind maps for Run 5 (PBL-BEM) showing the day and night mean wind patterns for the same period as Figure AF3.

References

Bi-Hui, Z., Shu-Hua, L., He-Ping, L., & Yan-Jun, M. (2012). The effect of MYJ and YSU schemes on the simulation of boundary layer meteorological factors of WRF. *Chinese Journal of Geophysics- Chinese Edition*, *55*, 2239–2248. https://doi.org/10.6038/j.issn.0001-5733.2012.07.010

Bougeault, P., & Lacarrere, P. (1989). Parameterization of Orography-Induced Turbulence in a Mesobeta–Scale Model. *Monthly Weather Review*, *117*(8), 1872–1890. https://doi.org/10.1175/1520-0493(1989)117<1872:POOITI>2.0.CO;2

C3S. (2018a). ERA5 hourly data on pressure levels from 1940 to present. https://doi.org/10.24381/CDS.BD0915C6

C3S. (2018b). ERA5 hourly data on single levels from 1940 to present. https://doi.org/10.24381/CDS.ADBB2D47

Chapman, L., Azevedo, J. A., & Prieto-Lopez, T. (2013). Urban heat & critical infrastructure networks: A viewpoint. *Urban Climate*, *3*, 7–12. https://doi.org/https://doi.org/10.1016/j.uclim.2013.04.001

Demuzere, M., Bechtel, B., Middel, A., & Mills, G. (2019). Mapping Europe into local climate zones (M. Mourshed, Ed.). *PLOS ONE*, *14*(4), e0214474. https://doi.org/10.1371/journal.pone.0214474

Demuzere, M., Kittner, J., & Bechtel, B. (2021). LCZ Generator: A Web Application to Create Local Climate Zone Maps. *Frontiers in Environmental Science*, *9*, 637455. https://doi.org/10.3389/fenvs.2021.637455

Dhakal, S., Minx, J., Toth, F., Abdel-Aziz, A., Figueroa Meza, M., Hubacek, K., Jonckheere, I., Kim, Y.-G., Nemet, G., Pachauri, S., Tan, X., & Wiedmann, T. (2022). Emissions Trends and Drivers [Section: 2]. In P. Shukla, J. Skea, R. Slade, A. A. Khourdajie, R. van Diemen, D. McCollum, M. Pathak, S. Some, P. Vyas, R. Fradera, M. Belkacemi, A. Hasija, G. Lisboa, S. Luz, & J. Malley (Eds.), *IPCC, 2022: Climate Change 2022: Mitigation of Climate Change. Contribution of Working Group III to the Sixth Assessment Report of the Intergovernmental Panel on Climate Change*. Cambridge University Press. https://doi.org/10.1017/9781009157926.004

Dirksen, M., Ronda, R. J., Theeuwes, N. E., & Pagani, G. A. (2019). Sky view factor calculations and its application in urban heat island studies. *Urban Climate*, *30*, 100498. https://doi.org/https://doi.org/10.1016/j.uclim.2019.100498

Esch, T., Brzoska, E., Dech, S., Leutner, B., Palacios-Lopez, D., Metz-Marconcini, A., Marconcini, M., Roth, A., & Zeidler, J. (2022). World Settlement Footprint 3D - A first three-dimensional survey of the global building stock. *Remote Sensing of Environment*, *270*, 112877. https://doi.org/10.1016/j.rse.2021.112877

European Environment Agency. (2020). CORINE Land Cover 2018 (raster 100 m), Europe, 6-yearly - version 2020_20u1, May 2020. https://doi.org/10.2909/960998c1-1870-4e82-8051-6485205ebbac
Accessed: November 19, 2024.

Fenner, D., Bechtel, B., Demuzere, M., Kittner, J., & Meier, F. (2021). Crowdqc+—a quality-control for crowdsourced air-temperature observations enabling world-wide urban climate applications. *Frontiers in Environmental Science*, *9*. https://doi.org/10.3389/fenvs.2021.720747

Foissard, X., & Fouvet, A.-C. (2022, November). *L'îlot de chaleur urbain grenoblois* (tech. rep.).

Grenoble Alpes Métropole. (2024). Grenoble Alpes Métropole Official Website. https://www.grenoblealpesmetropole.fr/
Accessed: 2024-11-09.

IGN. (2023). CoSIA: Couverture du Sol par Intelligence Artificielle. https://cosia.ign.fr/info#descriptif
Accessed: November 19, 2024.

Kapwata, T., Gebreslasie, M., & Wright, C. Y. (2022). An analysis of past and future heatwaves based on a heat-associated mortality threshold: Towards a heat health warning system. *Environmental Health*, *21*(1). https://doi.org/10.1186/s12940-022-00921-4

Kjellstrom, T., Briggs, D., Freyberg, C., Lemke, B., Otto, M., & Hyatt, O. (2016). Heat, Human Performance, and Occupational Health: A Key Issue for the Assessment of Global Climate Change Impacts [_eprint: https://doi.org/10.1146/annurev-publhealth-032315-021740]. *Annual Review of Public Health*, *37*(1), 97–112. https://doi.org/10.1146/annurev-publhealth-032315-021740

Largeron, Y., & Staquet, C. (2016). Persistent inversion dynamics and wintertime PM10 air pollution in Alpine valleys. *Atmospheric Environment*, *135*, 92–108. https://doi.org/https://doi.org/10.1016/j.atmosenv.2016.03.045

Le Bouëdec, E. (2021, December). *Wintertime characteristic atmospheric circulation in the Grenoble basin and impact on air pollution* (Publication No. 2021GRALU031) [Theses]. Université Grenoble Alpes [2020-....] https://theses.hal.science/tel-04148049

Martilli, A., Clappier, A., & Rotach, M. W. (2002). An Urban Surface Exchange Parameterisation for Mesoscale Models. *Boundary-Layer Meteorology*, *104*(2), 261–304. https://doi.org/10.1023/A:1016099921195

Martilli, A., Nazarian, N., Krayenhoff, E. S., Lachapelle, J., Lu, J., Rivas, E., Rodriguez-Sanchez, A., Sanchez, B., & Santiago, J. L. (2024). WRF-Comfort: Simulating microscale variability in outdoor heat stress at the city scale with a mesoscale model. *Geoscientific Model Development*, *17*(12), 5023–5039. https://doi.org/10.5194/gmd-17-5023-2024

Mason, H. M., King, J. C., Peden, A. E., & Franklin, R. C. (2022). Systematic review of the impact of heatwaves on health service demand in australia. *BMC Health Services Research*, *22*(1). https://doi.org/10.1186/s12913-022-08341-3

Meier, F., Fenner, D., Grassmann, T., Otto, M., & Scherer, D. (2017). Crowdsourcing air temperature from citizen weather stations for urban climate research. *Urban Climate*, *19*, 170–191. https://doi.org/https://doi.org/10.1016/j.uclim.2017.01.006

Météo-France. (2024). API Données Publiques Paquet Observation. https://portail-api.meteofrance.fr/web/fr/api/DonneesPubliquesPaquetObservation
Accessed: November 19, 2024.

Netatmo. (2024). Weather API Documentation. https://dev.netatmo.com/apidocumentation/weather#Available-data
Accessed: November 19, 2024.

Obradovich, N., Migliorini, R., Paulus, M. P., & Rahwan, I. (2018). Empirical evidence of mental health risks posed by climate change [_eprint: https://www.pnas.org/doi/pdf/10.1073/pnas.1801528115]. *Proceedings of the National Academy of Sciences*, *115*(43), 10953–10958. https://doi.org/10.1073/pnas.1801528115

Oke, T. R. (1982). The energetic basis of the urban heat island. *Quarterly Journal of the Royal Meteorological Society*, *108*(455), 1–24. https://doi.org/10.1002/qj.49710845502

OSM Buildings. (2024). OSM Buildings. https://osmbuildings.org/
Accessed: November 19, 2024.

Perkins, S. E., & Alexander, L. V. (2013). On the Measurement of Heat Waves. *Journal of Climate*, *26*(13), 4500–4517. https://doi.org/10.1175/JCLI-D-12-00383.1

Salamanca, F., Krpo, A., Martilli, A., & Clappier, A. (2010). A new building energy model coupled with an urban canopy parameterization for urban climate simulations—part I.

formulation, verification, and sensitivity analysis of the model. *Theoretical and Applied Climatology*, *99*(3-4), 331–344. https://doi.org/10.1007/s00704-009-0142-9

Theeuwes, N. E., Steeneveld, G.-J., Ronda, R. J., & Holtslag, A. A. M. (2017). A diagnostic equation for the daily maximum urban heat island effect for cities in northwestern Europe [_eprint: https://rmets.onlinelibrary.wiley.com/doi/pdf/10.1002/joc.4717]. *International Journal of Climatology*, *37*(1), 443–454. https://doi.org/https://doi.org/10.1002/joc.4717

Tong, S., Wang, X. Y., & Barnett, A. (2010). Assessment of heat-related health impacts in brisbane, australia: Comparison of different heatwave definitions. *PLoS ONE*, *5*(8), e12155. https://doi.org/10.1371/journal.pone.0012155

USGS. (2022). USGS EROS Archive—Land Cover Products—Global Land Cover Characterization (GLCC). https://doi.org/https://doi.org/10.5066/F7GB230D
Available online at https://www.usgs.gov/centers/eros/science/usgs-eros-archive-land-cover-products-global-land-cover-characterization-glcc.

Zhang, K., Rood, R. B., Michailidis, G., Oswald, E. M., Schwartz, J., Zanobetti, A., Ebi, K. L., & O'Neill, M. S. (2012). Comparing exposure metrics for classifying 'dangerous heat' in heat wave and health warning systems. *Environment International*, *46*, 23–29. https://doi.org/10.1016/j.envint.2012.05.001

Zumwald, M., Knüsel, B., Bresch, D. N., & Knutti, R. (2021). Mapping urban temperature using crowd-sensing data and machine learning. *Urban Climate*, *35*, 100739. https://doi.org/https://doi.org/10.1016/j.uclim.2020.100739